Nano Research
2020, 13(11): 2939–2949

ISSN 1998-0124 CN 11-5974/O4
https://doi.org/10.1007/s12274-020-2951-1

Research Article

Controllable optical emission wavelength in all-inorganic halide perovskite alloy microplates grown by two-step chemical vapor deposition

Mohammad K. Hossain[1,2], Pengfei Guo[5], Wayesh Qarony[4], Yuen H. Tsang[4], Chaoping Liu[6,7], Sai W. Tsang[3], Johnny C. Ho[3], and Kin M. Yu[1,3] (✉)

[1] *Department of Physics, City University of Hong Kong, Kowloon, Hong Kong SAR, China*
[2] *Department of Physics, Comilla University, Kotbari, Cumilla 3506, Bangladesh*
[3] *Department of Materials Science and Engineering, City University of Hong Kong, Kowloon, Hong Kong SAR, China*
[4] *Department of Applied Physics, The Hong Kong Polytechnic University, Hung Hom, Kowloon, Hong Kong SAR, China*
[5] *College of Physics and Optoelectronics, Taiyuan University of Technology, Taiyuan 030024, China*
[6] *Research Center for Advanced Optics and Photoelectronics, Department of Physics, College of Science, Shantou University, Shantou 515063, China*
[7] *Key Laboratory of Intelligent Manufacturing Technology of MOE, Shantou University, Shantou 515063, China*

Received: 18 April 2020 / **Revised:** 22 June 2020 / **Accepted:** 24 June 2020

ABSTRACT

All-inorganic halide perovskites (IHP), $CsPbX_3$ (X = Cl, Br, I) exhibiting efficient optical emissions within the spectral range of 410 to 730 nm are potential candidates for many optoelectronic devices. Anion alloying of these IHPs is expected to achieve tunable emission wavelength covering the entire visible spectrum. Here, we developed a two-step chemical vapor deposition (CVD) process for growing quaternary IHP $CsPbX_3$ (X = Cl/Br and Br/I) alloys. By exploiting the fast diffusion of halide anions in IHPs, the alloy composition can be precisely controlled by the growth time of the respective layers once the growth of the individual ternary IHP is optimized. Hence complexities in the multi-parameter optimization in the conventional CVD growth of quaternary alloys can be mitigated. Using this process, we synthesized single crystalline, homogeneous and thermally stable $CsPbCl_{3(1-x)}Br_{3x}$ and $CsPbBr_{3(1-x)}I_{3x}$ perovskites alloy microplates and demonstrated continuously tunable emission covering the spectrum from 428 to 715 nm by varying the halide compositions in the alloys. These alloy microplates also exhibit room temperature amplified spontaneous emissions (ASE) along with strong photonic discharges from the microplate's edges and hence are potentially useful as a gain medium as well as optical cavities for emissions with wavelengths covering the visible spectrum.

KEYWORDS

chemical vapor deposition, inorganic perovskites, quaternary alloys, emission spectrum, amplified spontaneous emissions (ASE)

1 Introduction

The recent rapid increase in the photovoltaic power conversion efficiency of organic hybrid halide perovskite (OHP) solar cells, from 3.8% (2009) to 25.2% (2020), has attracted great scientific and technological interests in these perovskite materials [1–6]. In addition to their great success in solar cell applications, these materials also possess many distinctive optical and electronic properties, including long electron hole diffusion lengths, tunable bandgap, low trap density and high charge carrier mobility [4, 7–13]. All these intriguing properties make them favorable materials for many optoelectronic applications such as lasers, light emitting diodes, photodetectors, waveguides, visible light communications, high sensitivity X-ray detectors, and sensors [11, 14–20]. In spite of their great promise in optoelectronic applications, the organic cation groups in these materials are especially vulnerable to moisture and heat, and hence achieving long term stable OHP based devices is still challenging [6, 21–25]. Such material instability strongly hinders the development and commercialization of a wide range of OHP optoelectronic devices. On the contrary, all-inorganic halide perovskites (IHP) show excellent resistance against open air oxygen, moisture and heat while still maintain most of the unique properties of their organic hybrid counterparts, and thus also have attracted much attention in recent years [14, 15, 21, 22, 26–31].

A wide bandgap tunability of a semiconductor can open opportunities for applications in new device architectures in optoelectronics. Therefore, in addition to their good optical properties, it is also desirable for IHPs to have a tunable bandgap, particularly over the entire visible spectrum [32–34]. Efficient optical emissions in the spectral range of 410 to 730 nm have been reported for $CsPbX_3$ (X = Cl, Br, I) perovskites [34, 35]. It is expected that alloying $CsPbX_3$ with different composition of anion halides can achieve tunable emission wavelength covering the entire visible spectrum. Moreover, it has also

Address correspondence to kinmanyu@cityu.edu.hk

been reported that the overall stability of halide perovskites can be improved by anion mixing [7, 23, 36, 37]. Such bandgap tunability in colloidal perovskite nanocrystals has been achieved via post-growth anion exchange [38]. Hence, the development of a proper growth process is necessary for exploiting bandgap tuning through precise composition control of inorganic halide perovskites [20, 36, 38–40].

In the last few years, owing to the versatile applications as well as superior optoelectronic and physiochemical properties, considerable efforts have been reported on IHPs with tunable compositions and optoelectronic properties [13, 33, 34, 41–45]. Most of these reports were based on materials synthesized by low cost and facile solution processing. However, these solution-synthesized materials usually suffer from poor crystalline quality and have high concentration of impurities from the precursors, solvents or surfactants used in the process [46, 47]. In addition, since the poor solubility limit of the metal halides restricts the solution growth of ternary $CsPbX_3$ alloy materials, therefore, it may be even a bigger challenge to synthesize bandgap tunable mixed anion quaternary alloys by this approach [20, 48]. On the contrary, it is well known that chemical vapor deposition (CVD) is a relatively simple, adaptable method for growing high quality single crystalline semiconductor materials and it has been utilized successfully for the synthesis of various perovskite materials [34, 47, 49]. For instance, Ha et al. reported an improvement of the electron diffusion length of the vapor phase grown $CH_3NH_3PbI_3$ nanoplatelets by a factor of two along with better optical properties and high crystallinity when compared to materials grown by solution process [50].

A major drawback of the CVD technique is that in order to optimize the materials properties several growth parameters have to be considered [51, 52]. Besides the growth temperature, other critical parameters including the physiochemical characteristics of the precursor materials like atomic mass, melting point, vapor pressure, etc., also play vital roles to the CVD growth [22, 37]. For quaternary IHP alloys with tunable bandgap, composition tuning is required. In the conventional single-step CVD, this requires a continuous change in the ratios of various precursors and therefore, and requires the optimization of the growth for each alloy composition. As a result, even for the same material system, tuning through the entire composition range may require numerous different growth optimization processes and thus making the growth time consuming and sometimes uncontrollable. Owing in part to the tedious growth optimization involved, there are only a few reports on the conventional CVD growth of halide perovskites [22, 34, 44, 47, 49]. In order to overcome this problem, Meyers et al. and Ha et al., reported a two-step CVD process for growing hybrid $CH_3NH_3PbI_3$ perovskite nanowires (NWs) and nanoplatelets [53, 54]. In this two-step process, PbI_2 structures were first grown, followed by the growth of CH_3NH_3I on top of the PbI_2 structures and finally the conversion into hybrid perovskite structures. Following the same two-step procedure, Xing et al. grew all three types of hybrid halide ($CH_3NH_3Pb(Cl, Br, I)_3$) perovskite NWs and reported their room temperature lasing [55]. However, so far these two-step CVD strategies are limited for the growth of ternary $CH_3NH_3Pb(Cl, Br, I)_3$ hybrid halide perovskites. No comprehensive investigation on this two-step CVD strategy for inorganic perovskites, in particular, compositionally tuned quaternary $CsPbCl_{3(1-x)}Br_{3x}$ and $CsPbBr_{3(1-x)}I_{3x}$ perovskite alloys has been reported.

In this work, we report on a systematic study of the synthesis of quaternary $CsPbCl_{3(1-x)}Br_{3x}$ and $CsPbBr_{3(1-x)}I_{3x}$ perovskite alloy microstructures using a two-step CVD process. The process exploits the fast diffusion of halide anions, facilitating the simultaneous formation of random alloys during growth. We demonstrate that using this process, it is only necessary to optimize the CVD growth of the respective end ternary $CsPbX_3$ compounds and the alloy composition can be precisely controlled by the growth time in each step. To achieve $CsPbCl_{3(1-x)}Br_{3x}$ and $CsPbBr_{3(1-x)}I_{3x}$ alloys with different composition, the growth of individual $CsPbX_3$ microstructures was first optimized and their growth rate characterized. Then, square like microplates (~ 5–25 μm) of $CsPbCl_3$ ($CsPbBr_3$) with the desired thickness were grown, followed by the growth of a top layer of $CsPbBr_3$ ($CsPbI_3$) for deposition time ranging from 0 to 25 (0–20) min. Interdiffusion of anions (Cl, Br and I) during the growth of the top $CsPbBr_3$ ($CsPbI_3$) overlayer results in the formation of uniform $CsPbCl_{3(1-x)}Br_{3x}$ ($CsPbBr_{3(1-x)}I_{3x}$) alloy microplates. The diffusion coefficients for Br and I in the corresponding alloys are found to be 3.36×10^{-11} and 6.73×10^{-11} $cm^2 \cdot s^{-1}$, respectively. Using this process, we successfully synthesized $CsPbX_3$ ($X = Cl_{1-x}Br_x$ and $Br_{1-x}I_x$) microplates with high crystalline quality on sapphire ($c\text{-}Al_2O_3$) and SiO_2/Si substrates. We found that the photoluminescence (PL) emission peak of these alloy microplates can be continuously tuned from 428 ($CsPbCl_3$) to 715 nm ($CsPbI_3$) (~ 2.9 to 1.7 eV) by controlling the $CsPbCl_{3(1-x)}Br_{3x}$ and $CsPbBr_{3(1-x)}I_{3x}$ alloy compositions. Moreover, room temperature amplified spontaneous emission (ASE) was observed in the as-grown alloy microplates. We note that these quaternary IHP alloy materials exhibit strong optical emissions over a large visible range, making them ideal materials for many optoelectronic applications. This two-step CVD process facilitates an easy way to precisely control the alloy composition and thus emission wavelength of these materials. It may also open up an opportunity for alloying other materials having completely different individual growth parameters suitable for photovoltaic and other optoelectronic applications.

2 Results and discussion

In our previous work, we reported the lasing and on-chip white light emissions in all-inorganic ternary lead halide perovskite, $CsPbX_3$ (X = Cl, Br, I) microplates grown by the CVD process [49]. However, the emission wavelength of these IHP materials have discrete values limited by their respective bandgap (2.91, 2.33, and 1.75 eV for X = Cl, Br and I, respectively). An alloy of $CsPbX_3$ with mixed anions can achieve an emission with any wavelength within the visible spectrum by controlling the ratio of the different anions. We explored the growth of mixed anion $CsPbX_3$ (Cl/Br, Br/I) at several anion ratio using a single-step CVD process and found that aside from the time-consuming growth parameter optimization, the composition of the deposited microstructures deviates significantly from the precursor composition. The details of the single- and two-step growth processes of the mixed anion halide perovskite alloy microstructures can be found in the experimental part. In the following sections we will first present results on the structure and composition and their variation with alloy composition of the quaternary alloys. Then the significant differences in the single- and two-step growths are discussed. The compositional uniformity and thermal stability of the two-step CVD grown alloys are studied. Finally, applications of these quaternary alloy microplates as gain medium and optical cavity are explored.

2.1 Microstructure and composition

Ternary $CsPbX_3$ (X = Cl, Br, I) alloys and their quaternary extensions $CsPbCl_{3(1-x)}Br_{3x}$ and $CsPbBr_{3(1-x)}I_{3x}$ alloys were grown by both single- and the newly designed two-step CVD strategies and were initially investigated by an optical microscope. Optical

images (Fig. S1 in the Electronic Supplementary Material (ESM)) clearly reveal that square like morphologies are dominating in the as grown perovskite samples. Scanning electron microscopy (SEM) images of $CsPbCl_{3(1-x)}Br_{3x}$ and $CsPbBr_{3(1-x)}I_{3x}$ alloy samples (Fig. 1(c), and Fig. S2 in the ESM) further reveal that the square like structures have smooth facets and sharp edges which suggest the single crystalline nature of the alloy materials. The lateral dimensions of the microplates vary between 5–25 μm with a thickness ranging from ~ 1.5 to ~ 3 μm. The dimensions can be varied by controlling the deposition time and the precursor contents. We note that there is a slight difference in the overall morphologies and microstructure distribution for alloy samples grown on c-plane sapphire (c-Al_2O_3) and SiO_2/Si substrates. Alloy samples grown on sapphire show microstructures with various morphologies including microplates of different shapes and tetrahedrons. The shapes of these microstructures suggest that most of them are precursors or aggregates of square microplates. A careful analysis suggests that ~ 50% of the microstructure are square-like microplates with dimension of a few to tens of μm. On the other hand, samples grown on SiO_2/Si substrate show much more uniform square microplate structures as seen in Fig. 1(c). We find that in the 2-step process, except for an increase in the structure thickness, the growth in step-2 does not alter the morphology of the structures formed in step-1. This occurs because the structures formed in the first growth act as nucleation sites for the second step growth. A similar phenomenon was also observed and reported earlier for the two-step vapor grown ternary hybrid halide perovskites nanoplatelets [50, 54].

The crystalline phase of the IHP alloys was studied by X-ray diffraction (XRD) using a BRUKER D2 Phaser. Pure $CsPbCl_3$, $CsPbBr_3$ and $CsPbI_3$ microplates are found to be tetragonal, monoclinic, and orthorhombic, respectively, similar to those reported previously for perovskite microstructures [47, 49]. Since the cubic phase is considered to be the high temperature phase of IHPs (for temperatures ≥ 47, 130, 305 °C for $CsPbCl_3$, $CsPbBr_3$ and $CsPbI_3$, respectively), the resulting room temperature crystal structures can be attributed to their subsequent phase transition when cooled down to room temperature after growth [47, 56]. Figure 1(d) shows that the strong (100) diffraction peaks from the $CsPbCl_3$ and $CsPbBr_3$ samples shift towards lower diffraction angles with increasing Br and I contents in the corresponding $CsPbCl_{3(1-x)}Br_{3x}$ and $CsPbBr_{3(1-x)}I_{3x}$ alloy lattices, respectively. This is consistent with an increase in the lattice parameter due to the substitution of the larger Br for Cl and I for Br in the anion sublattice. This demonstrates that the halide ions interdiffuse completely during growth and form random alloys with no phase separations. Taking the thickness of the step-1 grown alloy microstructure as the diffusion length L (section II in the ESM), we can roughly estimate the lower limit of the diffusion coefficient D for Br and I in the corresponding alloys by using the relation, $L = \sqrt{Dt}$, where t is taken as the overlayer growth time. The lower limit values for the diffusion coefficient D are estimated to be 3.36×10^{-11} and 6.73×10^{-11} $cm^2 \cdot s^{-1}$ for Br in $CsPbCl_3$ and I in $CsPbBr_3$, respectively.

We determine the composition of the alloy x by several methods. First, we estimate x by the change in the lattice parameter through the shift of the diffraction peak according to Vegard's law. The composition obtained from XRD is further confirmed by X-ray fluorescence (XRF) spectroscopy (EDAX Micro-XRF, Eagle-III). The XRF spectra reveal that the alloy microplates are composed of Cs, Pb, Cl, Br and Cs, Pb, Br, I (Fig. S3 in the ESM), respectively. Also, the atomic ratios obtained from XRF measurements suggest that the alloys have the correct ABX_3 stoichiometry with increasing halide ion substitution as the deposition time of the overlayer increases. In addition to XRD and XRF measurements, energy dispersive X-ray spectroscopy (EDS) in the scanning electron microscope was also performed on the $CsPbCl_{3(1-x)}Br_{3x}$ and $CsPbBr_{3(1-x)}I_{3x}$ alloy samples and the results are shown in Figs. 2(a) and 2(b), and Fig. S4 in the ESM. Several microplates were chosen on each type of alloy samples and EDS measurements were performed on at least three different locations on each microstructure. For both groups of alloy materials, EDS data obtained from different locations on the same square microplate show consistent composition, suggesting no compositional variation in the alloy microplates. Figure 2 shows examples of EDS analysis of 2 quaternary alloys, (a) $CsPbCl_{3(1-x)}Br_{3x}$ and (b) $CsPbBr_{3(1-x)}I_{3x}$ and the elemental mapping of these alloys. For $CsPbCl_{3(1-x)}Br_{3x}$ and $CsPbBr_{3(1-x)}I_{3x}$ alloy microstructures, the ratios of the respective elements are found to be Cs:Pb:(Cl:Br) = 18.2:17.54: (28.0:35.6) and Cs:Pb:(Br:I) = 20.6:19.8: (23.4:36.1), respectively

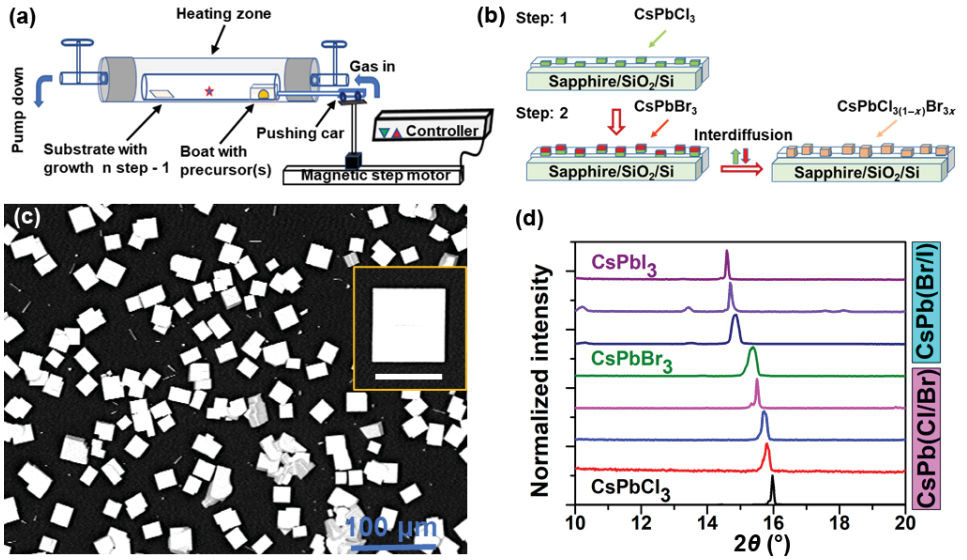

Figure 1 Growth and morphology of all-inorganic cesium lead halide perovskite alloy micro-plates. Schematics of (a) the CVD growth chamber and (b) the two-step alloy growth process. (c) SEM image of typical $CsPbCl_{3(1-x)}Br_{3x}$ alloy microplates grown on SiO_2/Si substrate, showing the smooth-clear surfaces, obtained from a 2-step CVD growth. The inset of (c) shows an enlarged image of one of the microplates (the scale bar is 20 μm). (d) XRD patterns from a series of $CsPbCl_{3(1-x)}Br_{3x}$ and $CsPbBr_{3(1-x)}I_{3x}$ alloy samples.

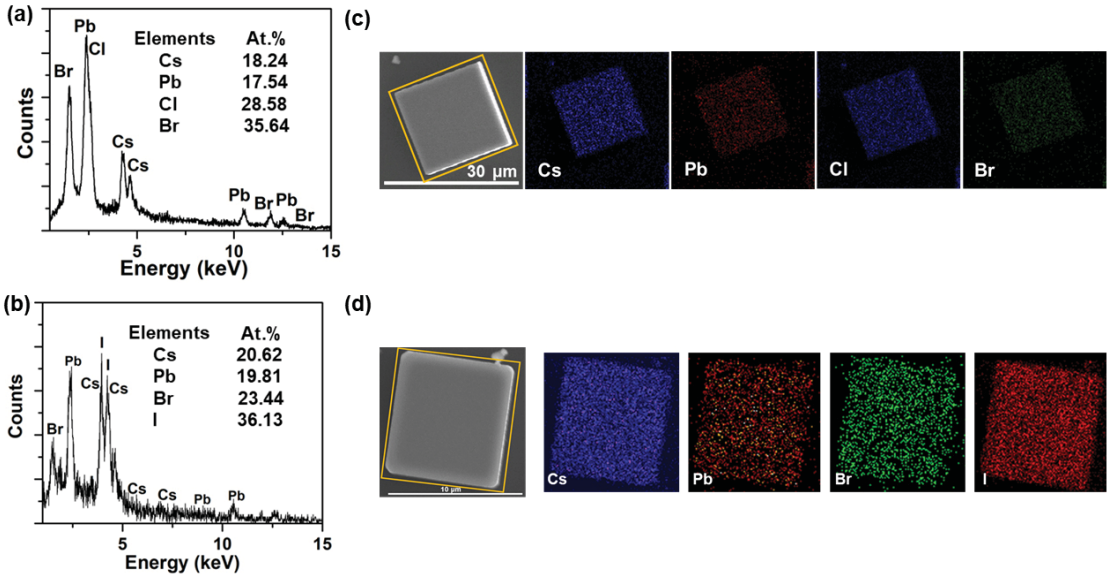

Figure 2 Compositional analysis of the two-step CVD grown cesium lead halide alloy microstructures. (a) and (b) EDS spectra of a $CsPbCl_{3(1-x)}Br_{3x}$ and a $CsPbBr_{3(1-x)}I_{3x}$ quaternary alloy microplates, respectively. The atomic ratio of various elements for the corresponding alloy are shown in the respective spectrum, indicating alloy stoichiometry of ABX_3. (c) and (d) SEM images and the elemental mapping of a $CsPbCl_{3(1-x)}Br_{3x}$ and a $CsPbBr_{3(1-x)}I_{3x}$ alloy microplates.

which closely support the ABX_3 formulation of the halide perovskites. Elemental mappings performed on a single square microplate of $CsPbCl_{3(1-x)}Br_{3x}$ (Fig. 2(c)) and $CsPbBr_{3(1-x)}I_{3x}$ (Fig. 2(d)) reveal no clustering of elements in specific regions, confirming the uniform lateral distributions of various elements throughout the surface of the alloy microstructures.

2.2 Bandgap tuning via varying the alloy composition

We compare properties of $CsPbCl_{3(1-x)}Br_{3x}$ and $CsPbBr_{3(1-x)}I_{3x}$ alloy microstructures grown by the two-step CVD process with those with similar composition grown by a single-step process. Room temperature PL measurements were performed on alloys grown by both processes and results are shown in Fig. 3. Figures 3(a) and 3(b) show the variation of the PL emission peaks with changing alloy composition from $CsPbCl_3 \rightarrow CsPbBr_3 \rightarrow CsPbI_3$ for the two-step and single-step CVD process, respectively. Real color emission photographs of the samples are also shown in the figures. We clearly observe emissions spanning continuously from violet (~ 2.9 eV; 428 nm $CsPbCl_3$) to green (~ 2.3 eV; 530 nm $CsPbBr_3$) to red (~ 1.7 eV; 715 nm $CsPbI_3$) attributed to the tunable $CsPbCl_{3(1-x)}Br_{3x}$ and $CsPbBr_{3(1-x)}I_{3x}$ alloy compositions.

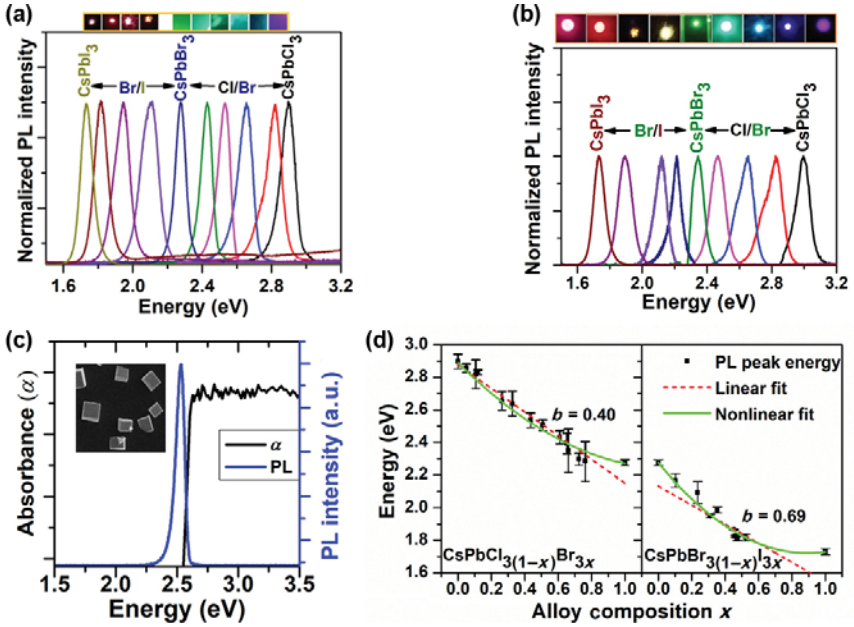

Figure 3 Optical properties of all-inorganic halide perovskite alloy microstructures. (a) and (b) PL spectra from a series of $CsPbCl_{3(1-x)}Br_{3x}$ and $CsPbBr_{3(1-x)}I_{3x}$ quaternary alloy microplates with different composition grown by the two-step and the conventional single-step CVD, respectively. Insets (top) are the real color emission from the corresponding alloy materials during PL measurements. (c) Room temperature absorbance and photoluminescence spectra of a typical $CsPbCl_{3(1-x)}Br_{3x}$ alloy sample with Br content, $x = 0.35$. Inset shows the SEM image of the alloy microstructure. (d) Change in bandgap with alloy composition (x) in two-step CVD grown halide perovskite alloys. The green lines represent fits of the data with the bandgap bowing Eqs. (2) and (3) respectively.

To correlate the material bandgap with the PL peak position, we performed spectrophotometry measurements in the spectral range from 200 to 1,700 nm. A direct comparison between the absorbance and PL spectra for a $CsPbCl_{3(1-x)}Br_{3x}$ alloy sample plotted in Fig. 3(c) shows that the PL peak position coincides with the absorption edge of the material, and hence the PL emission energy corresponds to the band gap of the material. Note that we cannot obtain the accurate absorption coefficient of the alloy since the probe beam size is much larger than the microplate sample and a large portion of the beam is passing through areas with no deposited structure. Figure 3(d) shows the variation in the band-edge energy (eV) obtained from the PL peak position as a function of different halide compositions (x), where x is the mole fraction for Br and I in the $CsPbCl_{3(1-x)}Br_{3x}$ and $CsPbBr_{3(1-x)}I_{3x}$ alloy system, respectively grown by the 2-step CVD process. The alloy composition x here is obtained from the XRD (100) diffraction peak according to Vegard's law and is found to be in good agreement with XRF and EDS data (Fig. S5 in the ESM). It is important to note that changes in alloy composition in the two-step CVD growths arise from the halide ion interdiffusion between the increasing thickness of the second layer grown with increasing time on top of the first bottom layer with a fixed thickness. For $CsPbCl_{3(1-x)}Br_{3x}$ and $CsPbBr_{3(1-x)}I_{3x}$, we find that with an increase in x (Br (I)) the bandgap of the alloy decreases monotonously from ~ 2.9 eV ($CsPbCl_3$) to ~ 1.7 eV ($CsPbI_3$). Typically, the bandgap of semiconductor alloys ($E_g(A_xB_{1-x})$) can be related to the bandgap values of the end point materials ($E_g(A)$ and $E_g(B)$) according to Vegard's Law with a small bowing parameter b,

$$E_g(A_xB_{1-x}) = xE_g(A) + (1-x)E_g(B) - bx(1-x) \quad (1)$$

For Cl/Br and Br/I alloys, the compositional dependence of the bandgap can be expressed as

$$E_g(CsPbCl_{3(1-x)}Br_{3x}) = (1-x)\cdot E_g(CsPbCl_3) + x\cdot E_g(CsPbBr_3) - b_{Cl/Br}\cdot x\cdot(1-x) \quad (2)$$

and

$$E_g(CsPbBr_{3(1-x)}I_{3x}) = (1-x)\cdot E_g(CsPbBr_3) + x\cdot E_g(CsPbI_3) - b_{Br/I}\cdot x\cdot(1-x) \quad (3)$$

Fitting the data in Fig. 3(d) with Eqs. (2) and (3), we obtain bowing parameters $b_{Cl/Br} = 0.4$ and $b_{Br/I} = 0.69$ eV. These bowing parameters are comparable to the previously reported result for $MAPbI_{3(1-x)}Br_{3x}$ OHP alloys with $b = 0.33$ [57].

2.3 Single-step vs. two-step CVD process

In the conventional single-step CVD, changing the composition of the alloy involves varying the ratio of the precursors of the component compounds in the source [52]. We note that the CVD growth process depends critically on the equilibrium vapor pressure of the reactant materials, which in turn is related to the molar ratio of the reactant materials in the precursor mixture. As a result, any small change in the precursor content may strongly affect the overall growth environment, resulting in a little or even no growth at all [58–60]. Therefore, during composition tuning, every different composition in the tunable range may require tedious growth optimization and thus making tuning the bandgap via composition variation a very challenging, or even a nonfeasible task. Figure 4(a) shows the alloy composition (x) for both $CsPbCl_{3(1-x)}Br_{3x}$ and $CsPbBr_{3(1-x)}I_{3x}$ alloys measured by XRD versus the composition (x) in the precursor mixture in the "optimized" conventional single-step CVD process. It can be observed that there are large deviations in the composition of the precursor mixtures and the microplates and that these deviations are neither constant nor linear. Figure 4(b) plots the difference of the precursor mixture composition and the composition of the microstructures. The difference in Br (ΔBr) and I (ΔI) contents in the respective powder sources and that in the as-grown alloy microplates are found to be ΔBr = 25%–70% for $CsPbCl_{3(1-x)}Br_{3x}$ and ΔI= 50%–80% for $CsPbBr_{3(1-x)}I_{3x}$. In general, the Br (I) composition in the precursor mixture is much higher than that measured in the deposited microstructures. This deviation is particularly severe in the mid composition region.

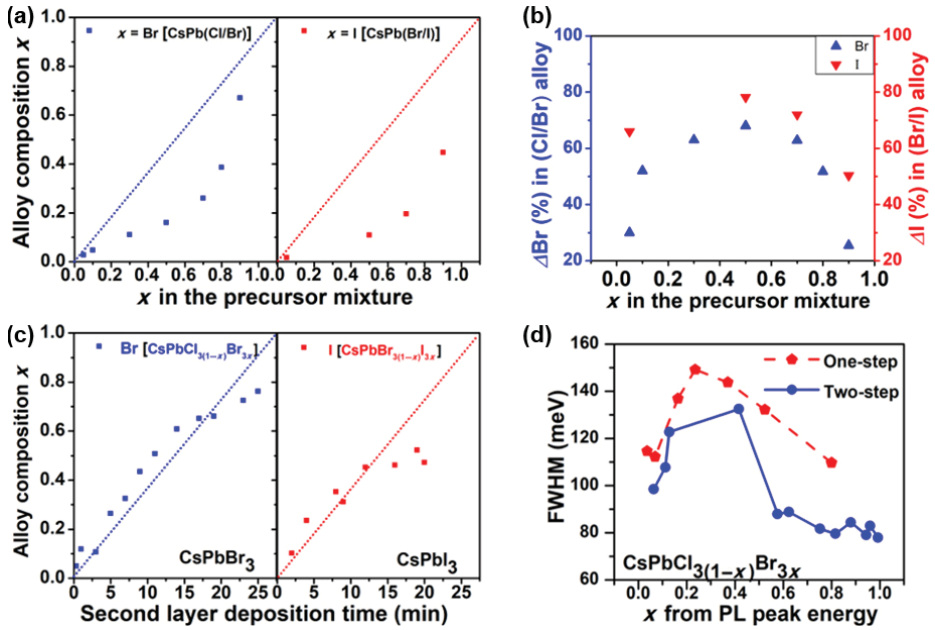

Figure 4 (a) Alloy composition (x) for both $CsPbCl_{3(1-x)}Br_{3x}$ and $CsPbBr_{3(1-x)}I_{3x}$ alloys measured by XRD versus the composition (x) in the precursor mixture in conventional single-step CVD growth. (b) Deviation of the halide composition in the alloy microplates from that of precursor mixtures, ΔBr and ΔI in conventional CVD growth. (c) Dependence of alloy composition (x) on the second layer deposition time (t) in a two-step CVD growth of $CsPbCl_{3(1-x)}Br_{3x}$ and $CsPbBr_{3(1-x)}I_{3x}$ alloys. (d) A comparison of the PL emission FWHM for $CsPbCl_{3(1-x)}Br_{3x}$ alloys with different composition grown by the single- and two-step CVD processes.

For comparison we show the alloy composition for $CsPbCl_{3(1-x)}Br_{3x}$ and $CsPbBr_{3(1-x)}I_{3x}$ alloys as a function of the second layer deposition time in the two-step CVD process in Fig. 4(c). In contrast to the single-step process, we observe a close to linear dependence of the microstructure composition on the deposition time of the second layer ($CsPbBr_3$ for the $CsPbCl_{3(1-x)}Br_{3x}$ and $CsPbI_3$ for $CsPbBr_{3(1-x)}I_{3x}$) in the two-step CVD growths. Here we emphasize that in the two-step CVD growth, growth optimizations have to be performed only on the end compounds ($CsPbCl_3$, $CsPbBr_3$ and $CsPbI_3$), and hence composition tuning is much simplified by just adjusting the growth time of the second layer.

Although both processes can achieve alloys with tunable composition, in the two-step CVD process by controlling the deposition time, we can precisely control the halide alloy composition, and thus resulting in a continuous PL peaks shifting. By adjusting the growth time of the second layer, we are able to control the change in the PL emission energy to 0.01 eV for $CsPbCl_{3(1-x)}Br_{3x}$ and 0.04 eV for $CsPbBr_{3(1-x)}I_{3x}$ alloys (Fig. S6 in the ESM). Moreover, when comparing PL emission peak of alloys grown by the 2 processes with similar composition, the peak width (FWHM) of the alloys grown with the two-step process is narrower than those grown by the single-step process. Overall, the FWHM of the PL emission peaks from the halide alloys grown by the two-step and the conventional single-step CVD are in the range of 80–120 and 85–150 meV, respectively. In particular, PL peak widths of alloys with $x > 0.5$ grown by the 2-step process are significantly narrower than those grown by the single-step process (with a difference in the peak width $\Delta_{FWHM} > 30$ meV). Since the PL peak width is an indication of the material quality and alloy composition uniformity [61], these results suggest that better material quality and/or compositional uniformity are achieved for alloys grown by the two-step CVD process. Figure 4(d) compares the PL peak width of $CsPbCl_{3(1-x)}Br_{3x}$ alloy samples grown by the 2 methods and clearly shows the higher quality materials grown by the two-step CVD process.

2.4 Composition uniformity: Vertical and lateral

In the two-step CVD process, the random alloy formation relies on the vertical interdiffusion of the halide ions between the layers formed by the 2 sequential growth. Therefore, it is important to verify that the vertical distribution of the halide ions is uniform throughout the sample. To address this issue, we carried out PL measurements with the laser illumination from the front and the back side of the microstructures on a series of $CsPbCl_{3(1-x)}Br_{3x}$ and $CsPbBr_{3(1-x)}I_{3x}$ alloy samples grown on double side polished sapphire substrates. In this experiment, the alloy composition was varied by first growing the $CsPbCl_3$ ($CsPbBr_3$) microstructures for 30(20) min, followed by a second step of $CsPbBr_3$ ($CsPbI_3$) growth for a time duration of 0 to 25 (0–20) min.

PL measurements were carried out with a 320 nm cw He-Cd laser as depicted in the schematic diagram in Fig. 5(a). The penetration depth of the laser can be estimated to be < 100 nm. Position dependent PL and PL obtained from both the front and back side illumination of the samples were collected for both groups of alloys. Figures 5(b) and 5(c) show plots of alloy composition estimated from the PL emission energy for both the front and back illumination measurements as a function of growth time of the $CsPbBr_3$ and $CsPbI_3$ overlayers, respectively for $CsPbCl_{3(1-x)}Br_{3x}$ and $CsPbBr_{3(1-x)}I_{3x}$ alloys. Here, the alloy composition is estimated from the PL peak energy by Vegard's law considering the bowing parameter $b_{Cl/Br} = 0.4$ and $b_{Br/I} = 0.69$ for $CsPbCl_{3(1-x)}Br_{3x}$ and $CsPbBr_{3(1-x)}I_{3x}$ alloys, respectively. In general, we find an excellent agreement on positions of the PL peaks obtained from the front and back illumination measurements on the same sample spot. This suggests that halide ions between the top and bottom layers intermixed completely, resulting in random alloys so that the front and back side of the layer has the same alloy composition. Error bars on the data points represent measurements from various spots on the sample surface. A direct comparison of PL spectra from the front and back side illuminations on a $CsPbCl_{3(1-x)}Br_{3x}$ and a $CsPbBr_{3(1-x)}I_{3x}$ alloys shown in the insets of Figs. 5(b)

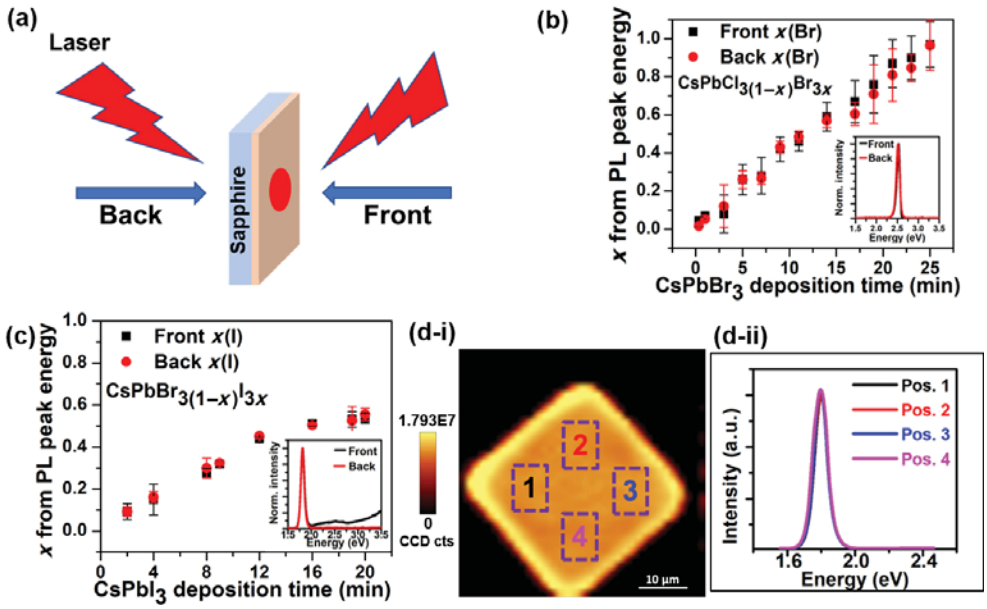

Figure 5 Vertical and lateral composition uniformity. (a) A schematic of the vertical uniformity measurement by photoluminescence (PL). (b) and (c) Alloy composition x as estimated from the PL emission energy for all-inorganic $CsPbCl_{3(1-x)}Br_{3x}$ and $CsPbBr_{3(1-x)}I_{3x}$ alloys, respectively obtained from the front and back illumination as a function of the second layer growth time. The insets show the front and back side PL spectra of a representative alloy sample of that particular alloy group. (d-i) μ-PL intensity mapping of typical $CsPbBr_{3(1-x)}I_{3x}$ alloy microplate for lateral uniformity study. (d-ii) Position dependent μ-PL spectra. μ-PL spectra taken from four different locations on the microplate surface showing identical PL position and intensity that reveals high lateral uniformity in the alloy microstructures.

and 5(c), respectively demonstrates the vertical composition uniformity along the growth direction.

The lateral uniformity of the alloy microplates was also investigated by PL intensity mapping performed on a typical $CsPbBr_{3(1-x)}I_{3x}$ microplate grown on sapphire (c-Al_2O_3) and the results are shown in Fig. 5(d). A WITec alpha300 R confocal Raman microscopy system equipped with a movable sample stage, a laser ($\lambda_{excitation}$ = 532 nm) and a digital camera were used for mapping randomly chosen square microplates in the sample. Since perovskite materials, especially the iodine-based perovskites are sensitive to laser illumination, a low laser power of 5.0 μW with mapping time of 5 min was adjusted carefully to avoid possible sample degradation and the resultant interference in the final PL output [62]. The PL intensity map is shown in Fig. 5(d-i) and PL spectra obtained from four different locations (as indicated in Fig. 5(d-i)) due to free excitonic emissions are shown in Fig. 5(d-ii). We observe that both the intensity and the peak widths of the PL emissions from different areas coincide. Moreover, the intensity distribution throughout the surface of the $CsPbBr_{3(1-x)}I_{3x}$ quaternary alloy microstructure is found to be quite uniform and no band tail is observed in the lower energy region of the PL spectra derived from the PL intensity map. These results clearly show that the composition of alloy microplate is laterally uniform and have high crystalline quality with very low density of crystalline defects [63, 64].

2.5 Ambient-air and thermal stability

Compared to the organic-hybrid counterparts, all-inorganic cesium lead halide perovskites are known to be more stable and resistant to moisture and temperature, making them suitable for real-world optoelectronic applications [31]. To study the stability of the quaternary IHP alloys against open air at room temperature, we performed PL measurements on typical $CsPbCl_{3(1-x)}Br_{3x}$ and $CsPbBr_{3(1-x)}I_{3x}$ alloy samples periodically for a time period of 14 months and results are shown in Fig. 6(a)(i, ii). Note that there is practically no change in the emission peak position. The FWHM of the PL peak (Fig. 6(a)(iii, iv)) for the $CsPbCl_{3(1-x)}Br_{3x}$ sample increases slightly from 90 to 120 meV while that of the $CsPbBr_{3(1-x)}I_{3x}$ sample stays constant at ~ 85 meV over the 10–14 months duration. The thermal stability of a typical $CsPbCl_{3(1-x)}Br_{3x}$ sample was also studied via isochronal (50–300 °C for 300 s) and isothermal (at 100 °C from 0 to 12 h) annealing in ambient air. The PL peak position and their corresponding FWHM of the annealed sample plotted in Fig. 6(b)(i, ii) reveal that in both annealing studies the alloys are very stable.

Photo-induced phase segregation has been reported for mixed halide perovskites [62, 65, 66], for example, $CsPbBr_{1.2}I_{1.8}$ nanocrystal ensemble film has been found to be unstable and phase separate under 30 W·cm^{-2} irradiations [62]. Therefore, it is also essential to study the stability of our all-inorganic mixed halide alloys under illumination. We note that we did not carry out an extensive investigation but just measured the alloys after our optical studies when the samples were exposed to long-term cw and pulsed laser irradiation during the steady state and the pumping power dependent PL measurements. Our measurements show no obvious change in the structure, morphology, and optical properties, confirming the high photo- and thermo-stability of these IHP alloys. During steady state PL measurements and other stability studies, the samples were exposed to laser power of ~ 100–190 mW·cm^{-2}, equivalent or higher than a normal AM1.5 one sun solar irradiation but several orders of magnitude lower than that used in the study of Zhang et al. [62]. Except for a slight change in the PL intensity, no photodegradation or photoinduced phase segregation can be detected. Photo-induced phase segregation of mixed halide perovskites has been suggested to proceed via grain boundaries, defects, and traps in the materials [62, 65, 67]. The photostability of our mixed halide perovskite microplates may be attributed to their low density of crystalline defects and single crystalline nature.

2.6 Quaternary alloy microplates as gain medium and optical cavity

Because of their chemical stability and excellent luminescence properties, IHP micro/nanostructures have been reported to be potential materials for lasing operations [34, 68, 69]. Also, the material morphology and crystalline quality can strongly influence the ASE performance [69]. Therefore, alloy microplates

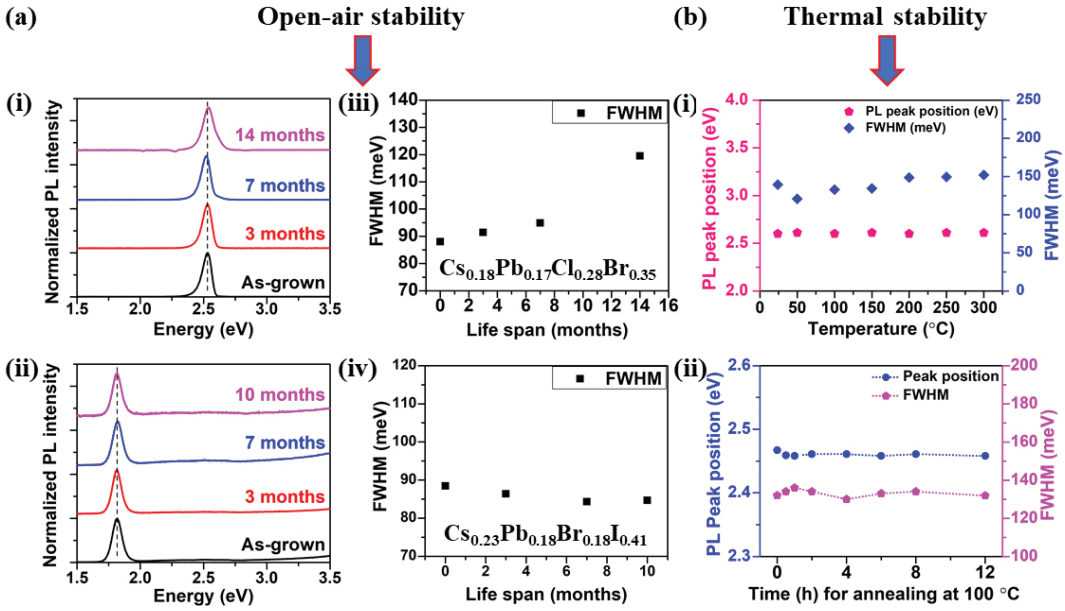

Figure 6 Stability of the two-step CVD grown halide perovskite alloy microplates studied by PL. (a) Room temperature open air stability, and (b) Thermal stability. Thermal stability was studied on a typical $CsPbCl_{3(1-x)}Br_{3x}$ alloy samples in two ways: (i) isochronal annealing for 300 s in the temperature range of 50 to 300 °C, and (ii) isothermal annealing at 100 °C for different time durations from 0–12 h.

with high crystalline quality, smooth mirror like surface, sharp clear edge and uniform-intense emission property should be ideal materials as optical cavities and also, should have an inherent lasing property.

To investigate the lasing properties of our quaternary alloy microplates, a laser scanning confocal microscope (Leica, TCS SP8) with a Ti: Sapphire femtosecond laser (Spectra-physics, Mai Tai HP; 80 MHz and 500 fs) excitation was used. The dedicated set up works on the principle of non-linear two-photon absorption (TPA)-based photo excitation which creates less photo-damage to the sample [69]. As depicted in the real color photograph of a $CsPbCl_{3(1-x)}Br_{3x}$ microplate shown in the inset of Fig. 7(a), the emission intensity around the microplate edges increases sharply with the increase in the power density, which is consistent with the wave guiding characteristic of the halide microplate under investigation. Figures 7(a) and 7(b) show the PL emission spectra and the emission peak intensity, respectively as a function of excitation power density. Region (i) in Fig. 7(b) shows an initial gradual linear increase in the emission peak intensity as the excitation power density increases up to a threshold power of ~ 0.8 mJ·cm^{-2}. Above this threshold power, the emission intensity increases sharply, indicative of ASE (region (ii)). However, the non-linearity curve resulted from stimulated emissions cannot be observed for our materials due to the limited excitation power of our system. Furthermore, along with increase in the PL intensity with increasing excitation power, the PL peak width (FWHM) shows a gradual decrease in Fig. 7(c). This further supports the lasing property of the halide alloy microplates [70]. We note that the modest Q value ($Q = \frac{\lambda}{\delta\lambda}$) of ~ 22 is due to the limited excitation power of our instrument so that the sharp stimulated emission peak cannot be observed at higher excitation power. Therefore, the high-quality quaternary alloy microplates grown by our two-step CVD can work simultaneously as a gain medium as well as an optical cavity which starts lasing at a certain threshold power. These whispering gallery mode (WGM) type cavity are important for many integrated photonic and optoelectronic applications where local modulation is a basic need for device operation. IHP alloy microplates can provide materials as WGM cavities over the entire visible emission spectrum.

The threshold power for ASE in our typical $CsPbCl_{3(1-x)}Br_{3x}$ alloy microcavity is 0.85 mJ·cm^{-2}, which is several orders of magnitude higher than that reported by Zhang et al. for $CsPbX_3$ (X =Cl, Br, I) nanoplatelets [68], but in good agreement with other reports on lasing thresholds for single crystal $CsPbBr_3$ materials [69, 71, 72]. It is apparent that the ASE threshold value strongly depends on the excitation source used in studying the lasing property of the halide perovskite materials. Experimentally, it has been observed that for the same nano/microstructure, the threshold power obtained for a two- or multi-photon excitation source is usually several orders of magnitude higher than that obtained by using a single-photon source [71, 72]. For example, using two-photon (λ = 800 nm) and three-photon (λ = 1,200 nm) excitations, Wang et al. obtained lasing thresholds of ~ 0.6 and 1.7 mJ·cm^{-2}, respectively for $CsPbBr_3$ nanorods [70]. To perform the lasing property study, our experimental setup employed a two-photon excitation source with λ_{exc} = 900 nm, and we obtained a lasing threshold of ~ 0.85 mJ·cm^{-2} for our $CsPbCl_{3(1-x)}Br_{3x}$ alloy microplate, similar to that observed by Wang et al. [70]. In contrast, Zhang et al. [68] used a single-photon excitation source with λ_{exc} = 400 nm and obtained a lasing threshold power density of ~ 2.2 μJ·cm^{-2} for IHP nanoplatelets. The higher lasing threshold power density for multiphoton excitation has been attributed to the much increased penetration depth due to lower absorptions of longer wavelength photons in the materials [71].

3 Conclusion

In summary, we have synthesized quaternary inorganic halide perovskite $CsPbX_3$ (X = Cl, Br and I) alloys using CVD methods and demonstrated continuously tunable emission covering the entire visible spectrum (from 428 to 715 nm) by varying the halide composition in the alloys. Moreover, we have developed a two-step CVD strategy for the growth of single crystalline, homogeneous and highly stable all-inorganic $CsPbCl_{3(1-x)}Br_{3x}$ and $CsPbBr_{3(1-x)}I_{3x}$ perovskites alloys. The new two-step CVD strategy exploits the fast diffusion of halide anions and mitigates complexities in the multi-parameter optimization in the conventional CVD process for the growth of quaternary alloys. Thus, alloy composition can be precisely controlled by the growth time of the respective layers once the growths of the individual ternary halide material are optimized. Microstructural characterization reveals that square like alloy microplates have smooth surface and sharp edges with a lateral dimension on the order of 10 μm and a thickness of around 2 μm. PL studies showed excellent optical properties of these $CsPbCl_{3(1-x)}Br_{3x}$ and $CsPbBr_{3(1-x)}I_{3x}$ alloys with uniform and intense blue to red emissions at room temperature. Excitation power dependent room temperature PL measurements suggest that the alloy microplates exhibit WGM lasing cavity behavior. Moreover, these IHP quaternary alloys exhibit improved thermal stability as well as resistance to oxygen, making them potential alternatives to organic hybrid perovskite materials for optoelectronic applications. This two-step CVD strategy may further open up opportunities for alloying other materials having completely different individual growth parameters suitable for photovoltaic and other optoelectronic applications.

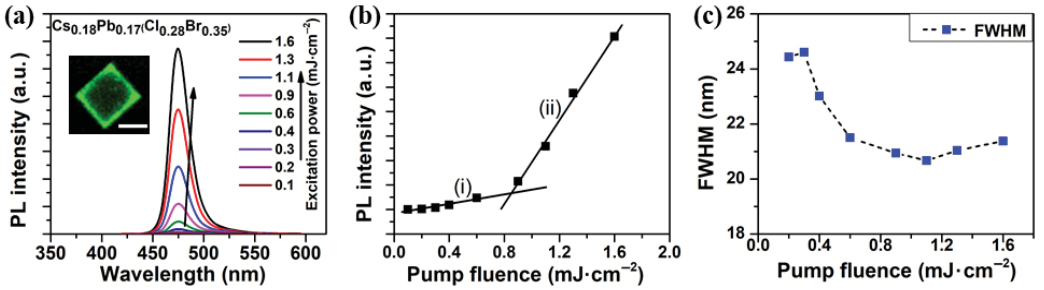

Figure 7 ASE in a typical $CsPbCl_{3(1-x)}Br_{3x}$ alloy sample. (a) Power dependent PL emission spectra. The inset is the cavity property of a typical $CsPbCl_{3(1-x)}Br_{3x}$ alloy microplate with a scale bar of 5 μm. (b) Non-linear response of PL intensity curve showing two-photon excited (λ_{exc} = 900 nm) amplified spontaneous emissions and (c) FWHM (nm) vs. pumping fluence (mJ·cm^{-2}) plot. A decrease in FWHM with pumping fluence validates the intrinsic ASE property of the halide materials.

4 Experimental

4.1 Growth of all-inorganic halide perovskite alloys microplates

4.1.1 *Growth parameters optimization for ternary alloys*

Growth parameters optimizations of the 3-end halide perovskite materials, $CsPbX_3$ (X = Cl, Br, I) were first carried out in order to perform the 2-step CVD growths of their quaternary alloys, $CsPbCl_{3(1-x)}Br_{3x}$ and $CsPbBr_{3(1-x)}I_{3x}$. A boron nitride (BN) boat loaded with PbX_2: CsX with a molar ratio 1:1 was introduced into the center of the furnace heating zone while c-Al_2O_3 (SiO_2/Si) substrates were placed at the downstream zone of the furnace. The system was first pumped down to a base pressure of < 20 mTorr by a mechanical pump, then high purity argon gas (Ar ~ 99.999%) at a flow rate of 100 sccm was introduced into the system for ~ 20 min to purge the tube. As soon as the furnace temperature reached its highest set value, the growth was initiated and continued for 10–60 min. The furnace was then allowed to cool down naturally to room temperature. During the $CsPbCl_3$ growth optimization, the temperature and pressure were varied respectively in the range between 540–600 °C and 4.6–5.0 Torr. The optimized parameter set for the growth of $CsPbCl_3$ microplates was found to be at 570 °C and an adjusted stable pressure with an Ar flow of 100 sccm, 4.8 Torr. Similar growth optimization procedures were followed for the growth of $CsPbBr_3$ and $CsPbI_3$ and the optimized sets were found to be (550 °C, 4.8 Torr) and (520 °C, 8.0 Torr), respectively.

4.1.2 *Single-step CVD growth of all-inorganic halide perovskite quaternary alloys*

During the single-step CVD growth of $CsPbCl_{3(1-x)}Br_{3x}$ alloys, mixed powders with the molar ratio $(1-x):x$ of ($PbCl_2$: CsCl) and ($PbBr_2$: CsBr)(molar ratio of 1:1 each) were loaded in a BN boat as the source of precursor materials. The boat was then placed at the center of the furnace while a number of c-Al_2O_3 (SiO_2/Si) substrates were placed in the downstream side of the heating zone of the furnace. Other procedures were maintained as discussed in section 4.1.1. For optimizing the growth of $CsPbCl_{3(1-x)}Br_{3x}$ alloys with different composition x, the furnace temperature was varied from 450–620 °C at a rate of 30 °C·min^{-1} with the pressure varied from 4.6–4.8 Torr. The same procedure was implemented for growing $CsPbBr_{3(1-x)}I_{3x}$ alloys except for replacing the precursors by ($PbBr_2$:CsBr) and (PbI_2:CsI) with successive changes in the iodine (I) contents. The corresponding growth temperature and pressure for $CsPbBr_{3(1-x)}I_{3x}$ alloys were in the range of 450–580 °C and 2.8–5.2 Torr, respectively. Note that for each composition x, a series of growths were carried out with different growth parameters to optimize the microplates growth, e.g., for growing $CsPbBr_{3(1-x)}I_{3x}$ microplates with x = 0.3, the ranges of temperature and pressure attempted were 450–480 °C and 2.0–7.8 Torr, respectively.

4.1.3 *Two-step CVD growth of all-inorganic halide perovskite quaternary alloys*

For the two-step CVD approach for growing $CsPbCl_{3(1-x)}Br_{3x}$ ($CsPbBr_{3(1-x)}I_{3x}$) alloys, we first grew $CsPbCl_3$ ($CsPbBr_3$) using 1:1 molar ratio of $PbCl_2$:CsCl ($PbBr_2$:CsBr) as precursor using the optimized parameters for a fixed deposition time of 30 (20) min to achieve a layer of $CsPbCl_3$ ($CsPbBr_3$) with a fixed thickness (on c-Al_2O_3 and SiO_2/Si substrates). A second layer of $CsPbBr_3$ ($CsPbI_3$) with 1:1 molar ratio of $PbBr_2$:CsBr (PbI_2:CsI) was then grown with the optimized growth parameters for a range of deposition time from 0 to 25 (0–20) min on top of the first grown layer of $CsPbCl_3$ ($CsPbBr_3$) microstructures to achieve $CsPbCl_{3(1-x)}Br_{3x}$ ($CsPbBr_{3(1-x)}I_{3x}$) alloy microplates with increasing x through halide ion interdiffusion. To minimize decomposition of the halide alloy structures grown in step-1, the growths in step-2 were conducted at a lower temperature than that of step-1. Table 1 summarizes the temperature profiles of step-1 and step-2 growths of the two-step CVD process for growing $CsPbCl_{3(1-x)}Br_{3x}$ and $CsPbBr_{3(1-x)}I_{3x}$ alloys. Also, in order to precisely control the growth time for the "Step-2" growth, we used a magnetic step motor controlled by a motion controller to introduce the source boat with the precursors for the second layer when the furnace temperature reached the desired optimized value. In this way the second layer thickness and in turn the alloy composition can be controlled.

Table 1 Temperature profiles of step-1 and step-2 growths of the two-step CVD process

Alloy composition	Step-1	Step-2
$CsPbCl_{3(1-x)}Br_{3x}$	$CsPbCl_3$ @ 570 °C	$CsPbBr_3$ @ 550 °C
$CsPbBr_{3(1-x)}I_{3x}$	$CsPbBr_3$ @ 550 °C	$CsPbI_3$ @ 520 °C

4.2 Structural, optical, and ASE characterizations

Microstructural information was obtained using an optical microscope (Olympus) and a scanning electron microscope (JEOL JSM 820). The X-ray diffraction measurement was performed using Bruker D2 Phaser that uses a Cu-Kα source having X-ray wavelength of 1.54184 Å. Di MultiModeV (Veeco) AFM measurement system controlled by NanoScopeV was used to see the morphology and to measure the dimensions of the alloy microplates. The growth rate of different halide compositions was then estimated from the thickness values and the corresponding deposition time. EDAX Micro XRF Eagle III was used for X-ray fluorescence spectroscopic analysis of the elements in the alloy materials. Also, the *in-situ* EDS of the SEM (JEOL JSM 820) was used for studying the chemical compositions, and the corresponding elemental mapping of the alloy samples was also performed.

A home-built PL system consisting of a 320 nm cw He-Cd laser source, a collimator, optical lens, and an ocean optics (USB 2000) spectrometer- was used to perform the steady state PL measurements. UV–vis–NIR spectroscopic measurements were performed by MProbe, thin film measurement system (Semiconsoft, Inc.) to study the transmittance of the alloy materials. Absorbance was calculated from the corresponding transmittance and the AFM measured thickness data. WITec alpha300 R confocal Raman microscopy facilitated μ-PL system was used for the lateral uniformity study. For studying the ASE of the alloy platelets, a laser scanning confocal microscopy system (Leica, TCS SP8) equipped with Ti: Sapphire femtosecond laser (Spectra-physics, Mai Tai HP) was used. The repetition rate of the laser pulse is 80 MHz and the corresponding duration of time is 500 fs. The hybrid detection system included in the laser scanning confocal microscopy was used to collect the nonlinear emissions from the experimental all-inorganic lead halide perovskite alloy samples.

Data availability

Data are available from the corresponding author only upon request.

Acknowledgements

This work was financially supported by CityU SGP (No. 9380076).

Electronic Supplementary Material: Supplementary material (including growth rate of halide ions, optical and SEM images, XFR spectra, EDS spectra, comparative compositional change (measured from XRF and XRD) with second layer deposition time graph, precise composition tuning graph, and change in bandgap with second layer deposition time graph, etc.) is available in the online version of this article at https://doi.org/10.1007/s12274-020-2951-1.

References

[1] Kojima, A.; Teshima, K.; Shirai, Y.; Miyasaka, T. Organometal halide perovskites as visible-light sensitizers for photovoltaic cells. *J. Am. Chem. Soc.* **2009**, *131*, 6050–6051.

[2] *NREL Best Research-Cell Efficiencies* [Online]. https://www.nrel.gov/pv/cell-efficiency.html (accessed April 16, 2020).

[3] Huang, H.; Polavarapu, L.; Sichert, J. A.; Susha, A. S.; Urban, A. S.; Rogach, A. L. Colloidal lead halide perovskite nanocrystals: Synthesis, optical properties and applications. *NPG Asia Mater.* **2016**, *8*, e328.

[4] Yin, W. J.; Yan, Y. F.; Wei, S. H. Anomalous alloy properties in mixed halide perovskites. *J. Phys. Chem. Lett.* **2014**, *5*, 3625–3631.

[5] Filip, M. R.; Eperon, G. E.; Snaith, H. J.; Giustino, F. Steric engineering of metal-halide perovskites with tunable optical band gaps. *Nat. Commun.* **2014**, *5*, 5757.

[6] Li, Z.; Yang, M. J.; Park, J. S.; Wei, S. H.; Berry, J. J.; Zhu, K. Stabilizing perovskite structures by tuning tolerance factor: Formation of formamidinium and cesium lead iodide solid-state alloys. *Chem. Mater.* **2016**, *28*, 284–292.

[7] Ning, C. Z.; Dou, L. T.; Yang, P. D. Bandgap engineering in semiconductor alloy nanomaterials with widely tunable compositions. *Nat. Rev. Mater.* **2017**, *2*, 17070.

[8] Kim, A.; Son, B. H.; Kim, H. S.; Ahn, Y. H. Direct measurement of diffusion length in mixed lead-halide perovskite films using scanning photocurrent microscopy. *Curr. Opt. Photonics* **2018**, *2*, 514–518.

[9] Eaton, S. W.; Lai, M. L.; Gibson, N. A.; Wong, A. B.; Dou, L.; Ma, J.; Wang, L. W.; Leone, S. R.; Yang, P. D. Lasing in robust cesium lead halide perovskite nanowires. *Proc. Natl. Acad. Sci. USA* **2016**, *113*, 1993–1998.

[10] Ahmadi, M.; Wu, T.; Hu, B. A review on organic-inorganic halide perovskite photodetectors: Device engineering and fundamental physics. *Adv. Mater.* **2017**, *29*, 1605242.

[11] Fu, Y. P.; Zhu, H. M.; Schrader, A. W.; Liang, D.; Ding, Q.; Joshi, P.; Hwang, L.; Zhu, X. Y.; Jin, S. Nanowire lasers of formamidinium lead halide perovskites and their stabilized alloys with improved stability. *Nano Lett.* **2016**, *16*, 1000–1008.

[12] Edri, E.; Kirmayer, S.; Cahen, D.; Hodes, G. High open-circuit voltage solar cells based on organic-inorganic lead bromide perovskite. *J. Phys. Chem. Lett.* **2013**, *4*, 897–902.

[13] Eperon, G. E.; Paternò, G. M.; Sutton, R. J.; Zampetti, A.; Haghighirad, A. A.; Cacialli, F.; Snaith, H. J. Inorganic caesium lead iodide perovskite solar cells. *J. Mater. Chem. A* **2015**, *3*, 19688–19695.

[14] Jiang, Y.; Leyden, M. R.; Qiu, L. B.; Wang, S. H.; Ono, L. K.; Wu, Z. F.; Juarez-Perez, E. J.; Qi, Y. B. Combination of hybrid CVD and cation exchange for upscaling Cs-substituted mixed cation perovskite solar cells with high efficiency and stability. *Adv. Funct. Mater.* **2018**, *28*, 1703835.

[15] Song, J. Z.; Li, J. H.; Li, X. M.; Xu, L. M.; Dong, Y. H.; Zeng, H. B. Quantum dot light-emitting diodes based on inorganic perovskite cesium lead halides ($CsPbX_3$). *Adv. Mater.* **2015**, *27*, 7162–7167.

[16] Yang, T.; Zheng, Y. P.; Du, Z. T.; Liu, W. N.; Yang, Z. B.; Gao, F. M.; Wang, L.; Chou, K. C.; Hou, X. M.; Yang, W. Y. Superior photodetectors based on all-inorganic perovskite $CsPbI_3$ nanorods with ultrafast response and high stability. *ACS Nano* **2018**, *12*, 1611–1617.

[17] Zhang, Y. P.; Liu, J. Y.; Wang, Z. Y.; Xue, Y. Z.; Ou, Q. D.; Polavarapu, L.; Zheng, J L. Qi, X.; Bao, Q. L. Synthesis, properties, and optical applications of low-dimensional perovskites. *Chem. Commun.* **2016**, *52*, 13637–13655.

[18] Dursun, I.; Shen, C.; Parida, M. R.; Pan, J.; Sarmah, S. P.; Priante, D.; Alyami, N.; Liu, J. K.; Saidaminov, M. I.; Alias, M. S. et al. Perovskite nanocrystals as a color converter for visible light communication. *ACS Photonics* **2016**, *3*, 1150–1156.

[19] Wei, H. T.; Fang, Y. J.; Mulligan, P.; Chuirazzi, W.; Fang, H. H.; Wang, C. C.; Ecker, B. R.; Gao, Y. L.; Loi, M. A.; Cao, L. et al. Sensitive X-ray detectors made of methylammonium lead tribromide perovskite single crystals. *Nat. Photonics* **2016**, *10*, 333–339.

[20] Aamir, M.; Adhikari, T.; Sher, M.; Khan, M. D.; Akhtar, J.; Nunzi, J. M. Cesium lead halide perovskite nanostructures: Tunable morphology and halide composition. *Chem. Rec.* **2018**, *18*, 230–238.

[21] Beal, R. E.; Slotcavage, D. J.; Leijtens, T.; Bowring, A. R.; Belisle, R. A.; Nguyen, W. H.; Burkhard, G. F.; Hoke, E. T.; McGehee, M. D. Cesium lead halide perovskites with improved stability for tandem solar cells. *J. Phys. Chem. Lett.* **2016**, *7*, 746–751.

[22] Park, K.; Lee, J. W.; Kim, J. D.; Han, N. S.; Jang, D. M.; Jeong, S.; Park, J.; Song, J. K. Light-matter interactions in cesium lead halide perovskite nanowire lasers. *J. Phys. Chem. Lett.* **2016**, *7*, 3703–3710.

[23] Nam, J. K.; Chai, S. U.; Cha, W.; Choi, Y. J.; Kim, W.; Jung, M. S.; Kwon, J.; Kim, D.; Park, J. H. Potassium incorporation for enhanced performance and stability of fully inorganic cesium lead halide perovskite solar cells. *Nano Lett.* **2017**, *17*, 2028–2033.

[24] Ju, M. G.; Dai, J.; Ma, L.; Zeng, X. C. Lead-free mixed tin and germanium perovskites for photovoltaic application. *J. Am. Chem. Soc.* **2017**, *139*, 8038–8043.

[25] Tenuta, E.; Zheng, C.; Rubel, O. Thermodynamic origin of instability in hybrid halide perovskites. *Sci. Rep.* **2016**, *6*, 37654.

[26] Seth, S.; Samanta, A. A facile methodology for engineering the morphology of $CsPbX_3$ perovskite nanocrystals under ambient condition. *Sci. Rep.* **2016**, *6*, 37693.

[27] Dastidar, S.; Egger, D. A.; Tan, L. Z.; Cromer, S. B.; Dillon, A. D.; Liu, S.; Kronik, L.; Rappe, A. M.; Fafarman, A. T. High chloride doping levels stabilize the perovskite phase of cesium lead iodide. *Nano Lett.* **2016**, *16*, 3563–3570.

[28] Xu, T. T.; Chen, L. X.; Guo, Z. H.; Ma, T. L. Strategic improvement of the long-term stability of perovskite materials and perovskite solar cells. *Phys. Chem. Chem. Phys.* **2016**, *18*, 27026–27050.

[29] Hoffman, J. B.; Schleper, A. L.; Kamat, P. V. Transformation of sintered $CsPbBr_3$ nanocrystals to cubic $CsPbI_3$ and gradient $CsPbBr_xI_{3-x}$ through halide exchange. *J. Am. Chem. Soc.* **2016**, *138*, 8603–8611.

[30] Li, X. M.; Cao, F.; Yu, D. J.; Chen, J.; Sun, Z. G.; Shen, Y. L.; Zhu, Y.; Wang, L.; Wei, Y.; Wu, Y. et al. All inorganic halide perovskites nanosystem: Synthesis, structural features, optical properties and optoelectronic applications. *Small* **2017**, *13*, 1603996.

[31] Zhang, L. Q.; Yang, X. L.; Jiang, Q.; Wang, P. Y.; Yin, Z. G.; Zhang, X. W.; Tan, H. R.; Yang, Y.; Wei, M. Y.; Sutherland, B. R. et al. Ultra-bright and highly efficient inorganic based perovskite light-emitting diodes. *Nat. Commun.* **2017**, *8*, 15640.

[32] Ndione, P. F.; Li, Z.; Zhu, K. Effects of alloying on the optical properties of organic-inorganic lead halide perovskite thin films. *J. Mater. Chem. C* **2016**, *4*, 7775–7782.

[33] Lei, T.; Lai, M. L.; Kong, Q.; Lu, D.; Lee, W.; Dou, L. T.; Wu, V.; Yu, Y.; Yang, P. D. Electrical and optical tunability in all-inorganic halide perovskite alloy nanowires. *Nano Lett.* **2018**, *18*, 3538–3542.

[34] Zhou, H.; Yuan, S. P.; Wang, X. X.; Xu, T.; Wang, X.; Li, H. L.; Zheng, W. H.; Fan, P.; Li, Y. Y.; Sun, L. T. et al. Vapor growth and tunable lasing of band gap engineered cesium lead halide perovskite micro/nanorods with triangular cross section. *ACS Nano* **2017**, *11*, 1189–1195.

[35] Stranks, S. D.; Snaith, H. J. Metal-halide perovskites for photovoltaic and light-emitting devices. *Nat. Nanotechnol.* **2015**, *10*, 391–402.

[36] Zhou, Z. Q.; Cui, Y.; Deng, H. X.; Huang, L.; Wei, Z. M.; Li, J. B. Modulation of electronic and optical properties in mixed halide perovskites $CsPbCl_{3x}Br_{3(1-x)}$ and $CsPbBr_{3x}I_{3(1-x)}$. *Appl. Phys. Lett.* **2017**, *110*, 113901.

[37] Gil-Escrig, L.; Momblona, C.; La-Placa, M. G.; Boix, P. P.; Sessolo, M.; Bolink, H. J. Vacuum deposited triple-cation mixed-halide perovskite solar cells. *Adv. Energy Mater.* **2018**, *8*, 1703506.

[38] Huang, H.; Bodnarchuk, M. I.; Kershaw, S. V.; Kovalenko, M. V.; Rogach, A. L. Lead halide perovskite nanocrystals in the research spotlight: Stability and defect tolerance. *ACS Energy Lett.* **2017**, *2*, 2071–2083.

[39] Pan, G. C.; Bai, X.; Yang, D. W.; Chen, X.; Jing, P. T.; Qu, S. N.; Zhang, L. J.; Zhou, D. L.; Zhu, J. Y.; Xu, W. et al. Doping lanthanide into perovskite nanocrystals: Highly improved and expanded optical properties. *Nano Lett.* **2017**, *17*, 8005–8011.

[40] Zhang, J.; Shang, M. H.; Wang, P.; Huang, X. K.; Xu, J.; Hu, Z. Y.; Zhu, Y. J.; Han, L. Y. n-type doping and energy states tuning in $CH_3NH_3Pb_{1-x}Sb_{2x/3}I_3$ perovskite solar cells. *ACS Energy Lett.* **2016**, *1*, 535–541.

[41] Protesescu, L.; Yakunin, S.; Bodnarchuk, M. I.; Krieg, F.; Caputo, R.; Hendon, C. H.; Yang, R. X.; Walsh, A.; Kovalenko, M. V. Nanocrystals of cesium lead halide perovskites ($CsPbX_3$, X = Cl, Br, and I): Novel optoelectronic materials showing bright emission with wide color gamut. *Nano Lett.* **2015**, *15*, 3692–3696.

[42] Zhang, D. D.; Eaton, S. W.; Yu, Y.; Dou, L. T.; Yang, P. D. Solution-phase synthesis of cesium lead halide perovskite nanowires. *J. Am. Chem. Soc.* **2015**, *137*, 9230–9233.

[43] Zhang, A. D.; Dong, C. Q.; Ren, J. C. Tuning blinking behavior of highly luminescent cesium lead halide nanocrystals through varying halide composition. *J. Phys. Chem. C* **2017**, *121*, 13314–13323.

[44] Huang, L.; Gao, Q. G.; Sun, L. D.; Dong, H.; Shi, S.; Cai, T.; Liao, Q.; Yan, C. H. Composition-graded cesium lead halide perovskite nanowires with tunable dual-color lasing performance. *Adv. Mater.* **2018**, *30*, 1800596.

[45] Wang, Y.; Li, X. M.; Zhao, X.; Xiao, L.; Zeng, H. B.; Sun, H. D. Nonlinear absorption and low-threshold multiphoton pumped stimulated emission from all-inorganic perovskite nanocrystals. *Nano Lett.* **2016**, *16*, 448–453.

[46] Pan, D. X.; Fu, Y. P.; Chen, J.; Czech, K. J.; Wright, J. C.; Jin, S. Visualization and studies of ion-diffusion kinetics in cesium lead bromide perovskite nanowires. *Nano Lett.* **2018**, *18*, 1807–1813.

[47] Wang, Y. L.; Guan, X.; Li, D. H.; Cheng, H. C.; Duan, X. D.; Lin, Z. Y.; Duan, X. F. Chemical vapor deposition growth of single-crystalline cesium lead halide microplatelets and heterostructures for optoelectronic applications. *Nano Res.* **2017**, *10*, 1223–1233.

[48] Cha, H.; Bae, S.; Jung, H.; Ko, M. J.; Jeon, H. Single-mode distributed feedback laser operation in solution-processed halide perovskite alloy system. *Adv. Opt. Mater.* **2017**, 5, 1700545.

[49] Guo, P. F.; Hossain, M. K.; Shen, X.; Sun, H. B.; Yang, W. C.; Liu, C. P.; Ho, C. Y.; Kwok, C. K.; Tsang, S. W.; Luo, Y. S. et al. Room-temperature red-green-blue whispering-gallery mode lasing and white-light emission from cesium lead halide perovskite ($CsPbX_3$, X = Cl, Br, I) Microstructures. *Adv. Opt. Mater.* **2018**, *6*, 1700993.

[50] Ha, S. T.; Su, R.; Xing, J.; Zhang, Q.; Xiong, Q. H. Metal halide perovskite nanomaterials: Synthesis and applications. *Chem. Sci.* **2017**, *8*, 2522–2536.

[51] Tavakoli, M. M.; Gu, L. L.; Gao, Y.; Reckmeier, C.; He, J; Rogach, A. L; Yao, Y.; Fan, Z. Y. Fabrication of efficient planar perovskite solar cells using a one-step chemical vapor deposition method. *Sci. Rep.* **2015**, *5*, 14083.

[52] Kumar, S.; Sahare, P. D.; Kumar, S. Optimization of the CVD parameters for ZnO nanorods growth: Its photoluminescence and field emission properties. *Mater. Res. Bull.* **2018**, *105*, 237–245.

[53] Meyers, J. K.; Kim, S.; Hill, D. J.; Cating, E. E. M.; Williams, L. J.; Kumbhar, A. S.; McBride, J. R.; Papanikolas, J. M.; Cahoon, J. F. Self-catalyzed vapor–liquid–solid growth of lead halide nanowires and conversion to hybrid perovskites. *Nano Lett.* **2017**, *17*, 7561–7568.

[54] Ha, S. T.; Liu, X. F.; Zhang, Q.; Giovanni, D.; Sum, T. C.; Xiong, Q. H. Synthesis of organic-inorganic lead halide perovskite nanoplatelets: Towards high-performance perovskite solar cells and optoelectronic devices. *Adv. Opt. Mater.* **2014**, *2*, 838–844.

[55] Xing, J.; Liu, X. F.; Zhang, Q.; Ha, S. T.; Yuan, Y. W.; Shen, C.; Sum, T. C.; Xiong, Q. H. Vapor phase synthesis of organometal halide perovskite nanowires for tunable room-temperature nanolasers. *Nano Lett.* **2015**, *15*, 4571–4577.

[56] Møller, C. K. Crystal structure and photoconductivity of casium plumbohalides. *Nature* **1958**, *182*, 1436.

[57] Zhou, Y. Y.; Zhou, Z. M.; Chen, M.; Zong, Y. X.; Huang, J. S.; Pang, S. P.; Padture, N. P. Doping and alloying for improved perovskite solar cells. *J. Mater. Chem. A* **2016**, *4*, 17623–17635.

[58] Zhao, Y. X.; Zhu, K. Organic-inorganic hybrid lead halide perovskites for optoelectronic and electronic applications. *Chem. Soc. Rev.* **2016**, *45*, 655–689.

[59] Liu, M. Z.; Johnston, M. B.; Snaith, H. J. Efficient planar heterojunction perovskite solar cells by vapour deposition. *Nature* **2013**, *501*, 395–398.

[60] Ono, L. K.; Wang, S. H.; Kato, Y.; Raga, S. R.; Qi, Y. B. Fabrication of semi-transparent perovskite films with centimeter-scale superior uniformity by the hybrid deposition method. *Energy Environ. Sci.* **2014**, *7*, 3989–3993.

[61] Paul, T.; Chatterjee, B. K.; Maiti, S.; Sarkar, S.; Besra, N.; Das, B. K.; Panigrahi, K. J.; Thakur, S.; Ghorai, U. K.; Chattopadhyay, K. K. Tunable cathodoluminescence over the entire visible window from all-inorganic perovskite $CsPbX_3$ 1D architecture. *J. Mater. Chem. C* **2018**, *6*, 3322–3333.

[62] Zhang, H. C.; Fu, X.; Tang, Y.; Wang, H.; Zhang, C. F.; Yu, W. W.; Wang, X. Y.; Zhang, Y.; Xiao, M. Phase segregation due to ion migration in all-inorganic mixed-halide perovskite nanocrystals. *Nat. Commun.* **2019**, *10*, 1088.

[63] Sun, L. F.; Zhang, X. M.; Liu, F. C.; Shen, Y. D.; Fan, X. F.; Zheng, S. J.; Thong, J. T. L.; Liu, Z.; Yang, S. A., Yang, H. Y. Vacuum level dependent photoluminescence in chemical vapor deposition-grown monolayer MoS_2. *Sci. Rep.* **2017**, *7*, 16714.

[64] Wang, X. H.; Ning, J. Q.; Zheng, C. C.; Zhu, B. R.; Xie, L.; Wu, H. S.; Xu, S. J. Photoluminescence and Raman mapping characterization of WS_2 monolayers prepared using top-down and bottom-up methods. *J. Mater. Chem. C* **2015**, *3*, 2589–2592.

[65] Barker, A. J.; Sadhanala, A.; Deschler, F.; Gandini, M.; Senanayak, S. P.; Pearce, P. M.; Mosconi, E.; Pearson, A. J.; Wu, Y.; Srimath Kandada, A. R.; et al. Defect-assisted photoinduced halide segregation in mixed-halide perovskite thin films. *ACS Energy Lett.* **2017**, *2*, 1416–1424.

[66] Brennan, M. C.; Draguta, S.; Kamat, P. V.; Kuno, M. Light-induced anion phase segregation in mixed halide perovskites. *ACS Energy Lett.* **2018**, *3*, 204–213.

[67] Bush, K. A.; Frohna, K.; Prasanna, R.; Beal, R. E.; Leijtens, T.; Swifter, S. A.; McGehee, M. D. Compositional engineering for efficient wide band gap perovskites with improved stability to photoinduced phase segregation. *ACS Energy Lett.* **2018**, *3*, 428–435.

[68] Zhang, Q.; Su, R.; Liu, X. F.; Xing, J.; Sum, T. C.; Xiong, Q. H. High-quality whispering-gallery-mode lasing from cesium lead halide perovskite nanoplatelets. *Adv. Funct. Mater.* **2016**, *26*, 6238–6245.

[69] Zhao, C. Y.; Tian, W. M.; Liu, J. X.; Sun, Q.; Luo, J. J.; Yuan, H.; Gai, B. D.; Tang, J.; Guo, J. W.; Jin, S. Y. Stable two-photon pumped amplified spontaneous emission from millimeter-sized $CsPbBr_3$ single crystals. *J. Phys. Chem. Lett.* **2019**, *10*, 2357–2362.

[70] Zhuang, X. J.; Ouyang, Y.; Wang, X. X.; Pan, A. L. Multicolor semiconductor lasers. *Adv. Opt. Mater.* **2019**, *7*, 1900071.

[71] He, H. J.; Ma, E.; Chen, X. Y.; Yang, D. R.; Chen, B. L.; Qian, G. D. Single crystal perovskite microplate for high-order multiphoton excitation. *Small Methods* **2019**, *3*, 1900396.

[72] Wang, X. X.; Zhou, H.; Yuan, S. P.; Zheng, W. H.; Jiang, Y.; Zhuang, X. J.; Liu, H. J.; Zhang, Q. L.; Zhu, X. L.; Wang, X. et al. Cesium lead halide perovskite triangular nanorods as high-gain medium and effective cavities for multiphoton-pumped lasing. *Nano Res.* **2017**, *10*, 3385–3395.